2023

Waste to treasure: Regeneration of porous Co-based catalysts from spent LiCoO2 cathode materials for efficient oxygen evolution reaction

Xiaoying Helen Lu

Chi Him Tsang

Waste to treasure: Regeneration of porous Co-based catalysts from spent LiCoO2 cathode materials for efficient oxygen evolution reaction

Journal:	*ACS Sustainable Chemistry & Engineering*
Manuscript ID	sc-2022-055343.R1
Manuscript Type:	Article
Date Submitted by the Author:	n/a
Complete List of Authors:	Bian, Haidong; Shenzhen Automotive Research Institute, Beijing Institute of Technology Wu, Wubin; Shenzhen University, College of Materials Science & Engineering Zhu, Yuanyi; Shenzhen Automotive Research Institute, BIT Tsang, Chi Him; Technological and Higher Education Institute of Hong Kong - Chai Wan Campus, Faculty of Science and Technology Xu, Jingyou; Shenzhen University Liao, Xingan; Shenzhen University Lu, Xiaoying; Technological and Higher Education Institute of Hong Kong Liu, Chen; Shenzhen University, College of Materials Science & Engineering zhang, zheming; Shenzhen Automotive Research Institute, BIT

Waste to treasure: Regeneration of porous Co-based catalysts from spent $LiCoO_2$ cathode materials for efficient oxygen evolution reaction

Haidong Bian [a, b], Wubin Wu [c], Yuanyi Zhu [a, b], Chi Him Tsang[d], Jingyou Xu [c], Xingan Liao [c], Xiao-Ying Lu [d,], Chen Liu [c,*] Zheming Zhang [a, b,*]*

[a] Shenzhen Automotive Research Institute, Beijing Institute of Technology, Shenzhen 518118, Guangdong, China

[b] National Engineering Laboratory for Electric Vehicles, Beijing Institute of Technology, Beijing 100081, Beijing, China

[c] Shenzhen Key Laboratory of Polymer Science and Technology, College of Materials Science and Engineering, Shenzhen University, Shenzhen 518055, PR China

[d] Faculty of Science and Technology, Technological and Higher Education Institute of Hong Kong, Hong Kong, PR China

KEYWORDS：spent Li-ion batteries, $LiCoO_2$, Co_9S_8, Co_3O_4, oxygen evolution reaction

ABSTRACT： The increasing demand for portable electronic devices and electric vehicles (EV) has triggered the rapid growth of rechargeable Li-ion batteries (LIBs) markets. However, in the near future, it is predicated a large amount of spent LIBs will be scrapped, imposing huge pressure on environmental protection and resources reclaiming. The effective recycling or regeneration of the spent LIBs not only relieves the environmental burdens but also avoids the waste of valuable metal resources. Herein, a porous Co_9S_8/Co_3O_4 heterostructure is successfully synthesized from the spent $LiCoO_2$ (LCO) cathode materials via a conventional hydrometallurgy and sulfidation process. The fabricated Co_9S_8/Co_3O_4 catalyst proves high catalytic activity towards oxygen evolution reaction (OER) in alkaline solution, with an overpotential of 274 mV to achieve the current density of 10 mA cm^{-2} and a Tafel slope of 48.7 mV dec^{-1}. This work demonstrates a facile regeneration process of Co-based electrocatalysts from the spent $LiCoO_2$ cathode materials for efficient oxygen evolution reaction.

SYNOPSIS**:** This study provides a facile strategy for regeneration of an efficient Co-based electrocatalyst towards electrochemical water splitting from the Li-ion batteries waste.

INTRODUCTION

As one of the most promising new energy techniques, rechargeable lithium-ion batteries (LIBs) have been widely used as energy storage devices, due to their high energy density, long cycle stability, low carbon emission and wide operating temperature.[1, 2] In 2021, the global lithium market was estimated to be more than 400 kilotons lithium carbonate equivalent (LCE), and is

expected to grow at a compound annual growth rate (CAGR) of 19.0% from 2022 to 2027.[3] The soaring lithium market is mainly ascribed to the increasing demand for the LIBs in electric vehicles (EVs). In general, the lifespan of rechargeable LIBs is about 5-8 years,[4, 5] after which the LIBs will eventually be scrapped. It has been estimated that the waste of the spent LIBs in vehicles is around 102,000 tons in 2020, which potentially reaches 7.8 million tons by 2040.[6] The spent LIBs not only contain some heavy metals but also toxic electrolytes (ethylene carbonate, lithium hexaflurophosphate and propylene carbonate etc.) and organic binders (polyvinylidene fluoride, PVDF)).[7] Thus, the inappropriate disposal of spent LIBs may cause a series of environmental issues, including air pollution, groundwater pollution and damage to ecosystems, which finally endangers human health. Meanwhile, some valuable metals in LIBs, such as lithium, cobalt, nickel and manganese, are of great value in the trade market, for instance, the price of Li_2CO_3 is US$78,502, Ni is US$33,305 and Co is US$82,160 per metric ton by April in 2022.[8] With the growing demand for LIBs, the price of these battery raw materials is still increasing. Therefore, much attention needs to be paid for effective recycling and regeneration of spent LIBs, from the view of environmental protection and resource utilizations.

Meanwhile, transition-metal-based compounds, especially the group VIII 3d metals of Fe, Co and Ni, are attractive as non-precious metal catalysts for electrochemical water oxidation reaction, due to their low cost, abundant resources, high activity, long-term durability and their excellent electronic properties.[9-12] For example, Zhang et al. [13] fabricated a series of hierarchical Co_3O_4 hollow nanoplates doped with different metal atoms and found that Fe-doped Co_3O_4 exhibited superior electrocatalytic properties for OER with an overpotential of 262 mV at 10 mA cm^{-2}. Wang et al. [14] synthesized single-atomic Mo dispersed Co_9S_8 nanoflakes and the advanced

catalyst exhibited pronounced water oxidation activities in universal pH conditions. Thus, the cathode materials of spent LIBs can be converted into Co-based, Ni-based or Fe-based catalysts for electrochemical water splitting via careful structure and composition design. In this work, we propose a novel strategy which combine conventional hydrometallurgy and sulfidation process to convert the spent $LiCoO_2$ (LCO) into porous Co_9S_8/Co_3O_4 heterostructures for efficient oxygen evolution reaction. In a typical hydrometallurgical process, the spent LCO was treated by oxalic acid and the extracted Co metals were precipitated in the state of cobalt oxalate (CoC_2O_4). The as-obtained CoC_2O_4 powders were then mixed with thioacetamide and annealed in Ar, resulting in a porous Co_9S_8/Co_3O_4 heterostructures. Benefiting from the hierarchical porous structure, Co_9S_8/Co_3O_4 catalyst exhibited outstanding OER activity with an overpotential of 274 mV at 10 mA cm^{-2}, and a Tafel slope of 48.7 mV dec^{-1}. This work demonstrates an efficient strategy to recycle and regenerate the spent LCO batteries for electrochemical oxygen evolution reaction.

EXPERIMENTAL SECTION

Preparation of porous Co_3O_4, Co/Co_3O_4 and Co_9S_8/Co_3O_4. The spent LCO LIBs were purchased from a portable source produced from a local new energy technology company (Hengchuang Co., Ltd, Shenzhen). Before manually dismantling, the spent LIBs were soaked in a 5 wt% NaCl solution to completely discharge and avoid short circuiting. The spent LCO materials were scratched and collected from the cathode, thoroughly rinsed by deionized (DI) water and ethanol several times, and then dried in oven. In a typical leaching process, the spent LCO was treated in a dilute oxalic acid (1.0 M) with a solid/liquid ratio of 4 g L^{-1},[15] and then stirred under 200 rpm at 80 ℃ for 2 h. After that, CoC_2O_4 was precipitated and then filtered,

dried in vacuum. For mesoporous Co_3O_4, the obtained CoC_2O_4 was annealed in muffle furnace at 350 ^oC for 2 h with a heating rate of 5 ^oC min^{-1}. For Co/Co_3O_4 fabrication, CoC_2O_4 was treated in N_2/10 vol% H_2 at 350 ^oC for 2 h with a heating rate of 5 ^oC min^{-1}. In a procedure to prepare Co_9S_8/Co_3O_4, CoC_2O_4 powder was mixed with thioacetamide (1/10, w/w) in Ar at 450 $^oC$for 2 h with a heating rate of 5 ^oC min^{-1}.

Material characterization. The morphology and structure of all the fabricated samples were examined by a field-emission scanning electron microscope (FEI PREO S(A5-112), transmission electron microscope (TEM, JEM-200 (JEOL)) and high-resolution transmission microscope (HRTEM) equipped with an EDX detector (Oxford INCA). Crystal structure of samples were recorded on a powder X-ray diffractometer (XRD, Rigaku) with Cu-Kα radiation (λ= 1.5405 Å). Chemical composition and chemical state of the samples were analyzed by an X-ray photoelectron spectroscope (XPS, VG ESCALAB 220i-XL) with all the peak positions calibrated with respect to the C1s peak at 284.8 eV. Thermogravimetric analysis (TGA) was used to confirm the stability and decomposition temperature of the fabricated CoC_2O_4. N_2 adsorption/desorption isotherms were recorded on a Quantachrome Nova 1200e Surface Area Analyzer at 77 K. Raman spectra were measured using a Renishaw 2000 Raman microscope with a laser wavelength of 532 nm.

Electrochemical measurements. All the electrochemical activities were performed on a Metrohm Autolab electrochemical workstation in a conventional three-electrode setup, with the fabricated sample as the working electrode, a saturated Ag/AgCl as the reference electrode, a Pt foil as the counter electrode. For the working electrode fabrication, 5 mg of the catalysts were dispersed into a mixed solvent of 1 mL isopropanol/water (4:1 *v/v*) and 100 μL 5 wt % Nafion solution. The catalytic ink was then gradually dripped on the surface of carbon paper (CP) with a

loading of ~ 1.0 mg cm^{-2}, followed by drying under infrared lamp. 1 M KOH (pH=13.8) electrolyte was bubbled with high purity Ar gas before the test. All the tests were conducted at the room temperature. Before the measurement of the catalysts, cyclic voltammetry (CV) from 0 to 0.8 V (vs. Ag/AgCl) at 100 mV s^{-1} were tested for 20 cycles to activate the electrode. The linear sweep voltammetry (LSV) from 0 to 0.8 V with a scan rate of 2 mV s^{-1} was applied to evaluate the activity of the obtained materials. All the data were recorded with *i*R-correction. The electrochemical surface area (ECSA) was determined by CV measurements with various scan rates. The current density was normalized by ECSA according to the equation of $I_{ECSA} = I/S_{ECSA}$, where I = current density, I_{ECSA} = normalized current density and $S_{ECSA} = C_{dl}/C_s$ (C_{dl} = double layer capacitance, C_s = 60 μF cm^{-2}). Electrochemical impedance spectroscopy (EIS) measurements were carried out with an amplitude of ±5 mV in the frequency range of 100 kHz - 0.01 Hz at the desired overpotential (η). The stability tests were performed by chronoamperometry measurements (*I-t* curves) at fixed overpotential over time. All potentials were converted to reversible hydrogen electrode (RHE) according to the equation below:

$$E\ (\text{vs RHE}) = \text{E (vs Ag/AgCl)} + 0.197 + 0.059 \times \text{pH}\ (=13.8)$$

where E (vs Ag/AgCl) was the recorded potential vs. Ag/AgCl electrode.

RESULTS AND DISCUSSIONS

Fig. 1a shows the typical recycling and regeneration process of the spent LCO batteries to Co-based catalysts. First, the collected LCO powders were dispersed in hot oxalic solution (1 M, 80 ℃) to extract the metal ions,[15] i.e., Li^+ and Co^{2+}. The leaching efficiency of Li and Co was confirmed from the inductively coupled plasma-optical emission spectrometry (ICP-OES). From

ICP-OES results shown in Fig. S1, the leaching efficiency of Li in the solution is over 98% after 90 min, while extracted Co^{2+} would react with $C_2O_4^{2-}$ ions and precipitate in the state of CoC_2O_4. Then, different annealing conditions were optimized for the target catalysts. Figs. S2 shows the typical XRD patterns of the spent $LiCoO_2$ (JCPDS #50-0653, Fig S2a) and CoC_2O_4•$2H_2O$ powders (JCPDS #25-0250, Fig. S2b)). XRD patterns of the as-obtained catalysts (Figs. 1b, S6, S8 and S10) show a set of diffraction peaks at 19°, 31.3°, 36.8° and 44.8°, which are indexed to the (111), (220), (311) and (400) planes of Co_3O_4 (JCPDS #43-1003), respectively. The peak at 44.3° is attributed to the (002) plane of Co (JCPDS #05-0727), while the peaks at 29.8°, 31.2°, 47.5° and 52.1° are associated to the (311), (222), (511) and (440) planes of Co_9S_8 (JCPDS #65-6801), respectively. SEM images demonstrate that the spent LCO powder shows granular structure with variable particle size (Fig. S3a), while the precipitated CoC_2O_4 powder exhibit typical orthorhombic crystal structure (Fig. S3b). When annealing in air, the CoC_2O_4 crystals gradually decompose to Co_3O_4 nanoparticles with an average particle size of 13.5 nm (Figs. 1c-d). When treated in N_2/10vol% H_2, CoC_2O_4 is transformed into Co/Co_3O_4 nanoparticles with an average particle size of ~ 36.8 nm (Figs. 1e-f). Following the sulphuration process, the nanoparticle morphology is preserved but particle size reduced to ~ 19.6 nm in average (Figs. 1g-h).

TGA result shows a weight loss at around 200 ℃ (Fig. S4), which is ascribed to the loss of crystal water in CoC_2O_4•$2H_2O$.[15] The observed weight loss at ~ 300 ℃ is mainly due to the decomposition reaction of CoC_2O_4 to Co_3O_4.[15] Such results reveal that annealing temperature should be optimized for porous structure generation, as too high temperature would coarsen the structure and too low temperature would cause incomplete decomposition of CoC_2O_4. Temperature-dependent experiment was also carried out in order to further evaluate the

morphology and structure evolution during annealing in air and N_2/10vol% H_2. At low temperature in air (250 ℃ 2 h), lath-shaped microstructure is observed in some of regions (Figs. S5a-b). The lath structure is attributed to the incomplete decomposition of CoC_2O_4 crystals, which is also indicated from the corresponding XRD results (Grey line in Fig. S6). With gradually increasing the annealing temperature, the mean particle size of the sample increases from 13.5 nm at 350 ℃ (Fig 1d) to 50.4 nm at 650 ℃ (Figs. S5d-l). The phase structure of Co_3O_4 can be confirmed from XRD patterns (Fig. S6). Similar phenomenon is observed when CoC_2O_4 being treated in N_2/10 vol% H_2 (Fig. S7). The retained orthorhombic crystal morphology (Fig. S7a-b) and phase structure (Fig. S8) both suggest the presence of CoC_2O_4 at annealing temperature of 250 ℃. At higher annealing temperature, all the samples show granular microstructures with mean particle size increasing from 36.8 nm at 350 ℃ (Fig 1f) to 610 nm at 650 ℃ (Fig. S7d-l). XRD patterns show that Co_3O_4 is completely transformed to metallic Co phase at temperature higher than 450 ℃ (Fig. S8). To optimize the sulphuration parameters, the temperature and thioacetamide content are considered. Incomplete decomposition of CoC_2O_4 is observed at 350 ℃ (Fig. S10) with an average particle size of 17.1 nm (Fig S9a-c), while higher temperature at 550 ℃ incurs metallic Co phase (Fig. S10) and big particle size of ~ 120 nm (Fig. S9d-f). Co_9S_8 is formed with increasing the mixture of CoC_2O_4/thioacetamide (1/15, w/w) in Ar at 450 ℃, exhibiting a hierarchical structure with an average size of 20.5 nm (Fig. 9g-i).

The detailed morphology and microstructure of the samples were further investigated by transmission electron microscopy (TEM) and high-resolution TEM (HRTEM). As shown in Fig. 2a-b, the prepared Co_3O_4 shows a mesoporous structure, which comprises of subunits with an average size of 12.3 nm, consistent with previous SEM observation. The clear lattice fringe of 0.244 nm matches well with (311) plane of Co_3O_4 (Fig. 2c).[16] For Co/Co_3O_4 and Co_9S_8/Co_3O_4,

the mesoporous structure is also observed but with growing subunits (Figs. 2d-e and Figs. 2g-h). The lattice spacing of 0.244 nm, 0.155 nm and 0.216 nm correspond to the (311), (511) planes of Co_3O_4, and (100) plane of Co, respectively.[17, 18] A clear interface between Co and Co_3O_4 is observed, suggesting the Co is *in-situ* reduced on the surface of Co_3O_4 in N_2/10 vol% H_2. The formed Co/Co_3O_4 interface belongs to a typical Schottky junction, which can enhance the surface charge density of interfacial metals for improving the catalytic activity.[19] For Co_9S_8/Co_3O_4, the lattice spacing of 0.30 nm, 0.175 nm and 0.20 nm are assigned to the (311), (440) planes of Co_9S_8,[20] and (400) plane of Co_3O_4,[21] respectively. Clearly interface observed between Co_9S_8 and Co_3O_4 will accelerate the charge transfer across the interface and increase active sites, thus, contributing an improved electrocatalytic process.[22] The dark-field TEM image and the corresponding energy dispersive X-ray (EDX) element mapping images were recorded to confirm the elements in the samples. For Co_9S_8/Co_3O_4, a uniform distribution of Co, S and O elements over the whole structure is observed (Figs. 2j-m), suggesting the presence of a homogeneous Co_9S_8/Co_3O_4 interface in the sample. The EDX mapping results of Co_3O_4 and Co/Co_3O_4 also demonstrate the existence and distribution of Co and O in the sample, as shown in Fig. S11.

The survey spectra of X-ray photoelectron spectroscopy (XPS) of Co_3O_4 and Co/Co_3O_4 (Fig. 3a) also confirm the existence of Co and O, while Co_9S_8/Co_3O_4 is composed of Co, S and O. In the Co2p spectra of all samples, the peaks at 781.7 and 797.9 eV, 780.0 and 796.2 eV are reflected to Co $2p_{3/2}$ and $2p_{1/2}$ of Co^{2+} in Co_3O_4, Co $2p_{3/2}$ and $2p_{1/2}$ of Co^{3+} in Co_3O_4, respectively, while the peaks at 786.6 and 803.5 eV are accredited to the satellite peaks of Co^{2+}.[23-25] For Co/Co_3O_4, two new peaks located at 778.1 and 794.0 eV are accredited to the Co $2p_{3/2}$ and $2p_{1/2}$ spin orbitals of the Co^0, respectively, due to the existence of metallic Co in the sample.[26] For

Co_9S_8/Co_3O_4, the peaks with binding energies of 778.3 and 793.7 eV can be attributed to Co $2p_{3/2}$ and $2p_{1/2}$ from cobalt sulfides.[27, 28] In the deconvoluted S 2p spectrum of Co_9S_8/Co_3O_4 (Fig. 3c), the peaks located at 162.0 and 163.6 eV can be assigned to S $2p_{3/2}$ and $2p_{1/2}$ of Co-S bonds in Co_9S_8.[14] The peak evolves at 168.8 eV can be ascribed to the oxidized S species (SO_x^{n-}), implying easily surface oxidation of Co_9S_8 in air atmosphere.[29, 30] As for the O 1s spectra (Fig. 3d), the raw curves can be peak-fitted into three peaks located at 530.1, 531.7 and 533.8 eV, which can be assigned to the lattice oxygen (O_L) of Co-O, oxygen vacancies (O_V) and surface adsorbed hydroxyl groups, respectively.[24, 31, 32] In comparison to Co_3O_4, Co/Co_3O_4 and Co_9S_8/Co_3O_4 show obvious higher peak intensity at 531.7 eV, implying the significant improved concentration of O_V. The existence of O_V can provide unsaturated coordination sites for accelerated charge transfer and enhanced conductivity of the catalysts, thus facilitating the OER electrochemical performance.[31, 32]

The nitrogen adsorption-desorption isotherm curves of Co_3O_4, Co/Co_3O_4 and Co_9S_8/Co_3O_4 were depicted in Fig. 3e. All the curves show a typical Type IV characteristics with a hysteresis loop, demonstrating the presence of porous structures in all samples. The BET (Brunauer-Emmett-Teller) calculation indicates the Co_3O_4 has the largest surface area of 51.2 $m^2 g^{-1}$, while Co/Co_3O_4 and Co_9S_8/Co_3O_4 exhibit a surface area of 20.9 and 34.7 $m^2 g^{-1}$, respectively. The decreased surface area of Co/Co_3O_4 and Co_9S_8/Co_3O_4 may be ascribed to their increased subunits. Besides, the pore size distribution was obtained by density functional theory (DFT) method (Fig. 3f). All samples show mixed pores in the range of 15-100 nm, indicating the hierarchical porous structure (mesopores and macropores) of the sample. The hierarchical porous architecture with the heterojunction structure, has great influence on the mass and electron transportation during electrochemical reactions. Compared to Co/Co_3O_4, some of pores below 15

nm are observed for Co_3O_4 and Co_9S_8/Co_3O_4, which maybe another reason for a large surface area.

The electrocatalytic OER performance of the recycled Co-based catalysts were evaluated in a three-electrode cell in 1.0 M KOH. The polarization curves were tested by linear sweep voltammetry (LSV) with a scan rate of 2 mV s^{-1}. As shown in Figs. 4a and S14a-b, Co_9S_8/Co_3O_4 exhibits the best catalytic performance with a η_{10} (overpotential to achieve the current density of 10 mA cm^{-2}) of 274 mV, which is lower than that of Co_3O_4 (342 mV), Co/Co_3O_4 (298 mV), RuO_2 (293 mV), Co/Co_9S_8 (302 mV), Co_9S_8 (311 mV) and most of the reported Co-based electrocatalysts in alkaline electrolyte (Fig. 4b and Table S1). At large current densities (>50 mA cm^{-2}), Co_9S_8/Co_3O_4 also displays remarkable OER performance. It delivers a η_{100} (overpotential to achieve the current density of 100 mA cm^{-2}) of 335 mV, which is much lower than that of Co_3O_4 (417 mV), Co/Co_3O_4 (362 mV) and RuO_2 (390 mV). It is also notable that Co/Co_3O_4 exhibits better catalytic performance than RuO_2 at high current density (>50 mA cm^{-2}), which may be ascribed to the hierarchical porous architecture and presence of Schottky junction in Co/Co_3O_4. The electrocatalytic OER activity of air-treated and N_2/10 vol% H_2-annealed samples at 250-650 ℃, thioacetamide-treated samples at 350 and 550 ℃, and Co_9S_8 were also evaluated, as shown in Figs. S12-14. The sample treated in air and N_2/10 vol% H_2 at 350 ℃ exhibits the best OER performance, either too low or too high annealing temperature would deteriorate the catalytic performance of the electrode. Similar result is also observed for thioacetamide-treated sample at 350-550 ℃ (Fig. S14). The Tafel slope derived from LSV curve was also applied to evaluate the OER kinetics of prepared samples (Figs. 4c and S14c). The Co_9S_8/Co_3O_4 shows the lowest Tafel slope with a value of 48.7 mV dec^{-1}, while Co_3O_4, Co/Co_3O_4, RuO_2, CP (carbon paper), Co/Co_9S_8 and Co_9S_8 exhibit a Tafel slope of 70.5, 58.6, 57.6, 187.6, 62.9 and 78.1 mV

dec^{-1}, respectively. The lower Tafel slope of Co_9S_8/Co_3O_4 suggests the faster OER kinetics than Co_3O_4, Co/Co_3O_4, RuO_2, CP, Co/Co_9S_8 and Co_9S_8.

To better understand the OER activity of the prepared samples, the electrochemical active surface area (ECSA) was evaluated by electrochemical double layer capacitance (C_{dl}) based on the cycle voltammetry (CV) curves at different scan rates. Fig. 4d shows the CV curves of Co_9S_8/Co_3O_4 measured in the potential range of 0.875-0.975 V (*vs.* RHE) with a scan rate from 0.01 to 0.1 V s^{-1}. The C_{dl} of Co_9S_8/Co_3O_4 is calculated to be 12.5 mF cm^{-2}, which is nearly 3 times higher than that of Co/Co_3O_4 (4.8 mF cm^{-2}) and about 6 times higher than that of Co_3O_4 (2.1 mF cm^{-2}) and RuO_2 (2.4 mF cm^{-2}) (Fig. 4e). Figs. S15-S16 show the CV curves of air-annealed and N_2/10 vol% H_2-annealed samples and their corresponding ECSA results. It is clearly observed that the samples annealed at 350 ℃ both in air and N_2/10 vol% H_2 show the largest C_{dl}, either higher or lower annealing temperature result in a lower C_{dl}. The CV curves and corresponding ECSA results also confirm the higher C_{dl} of Co_9S_8/Co_3O_4 than that of Co_9S_8 and Co/Co_9S_8 (Fig. S17). It should be mentioned that the surface area (BET results) is not consistent with the ECSA results, which is probably associated with the heterostructures in Co/Co_3O_4 and Co_9S_8/Co_3O_4. Heterostructured catalysts usually possess more active sites than their single counterpart.[33] Furthermore, the ECSA-normalized LSVs were plotted (Fig. S18) and the results also demonstrated the higher intrinsic activity in Co_9S_8/Co_3O_4.

Electrochemical impedance spectroscopy (EIS) was applied to evaluate the electron transfer kinetics of the catalysts. Fig. 4f shows the Nyquist plot fitted with an equivalent circuit (inset in Fig.4f) of Co_3O_4, Co/Co_3O_4 and Co_9S_8/Co_3O_4. A unified electrolyte solution resistance (R_s) of 3.5-5 Ω is observed for all samples. Co_9S_8/Co_3O_4 shows a fitting charge transfer resistances (R_{ct}) of 34.7 Ω, which is much lower than that of Co_3O_4 (60.4 Ω) and Co/Co_3O_4 (121 Ω). The low R_{ct}

value of Co_9S_8/Co_3O_4 indicates an excellent OER kinetics and a high charge-transfer rate at the electrolyte/catalysts interface. Chronoamperometry at an overpotential of 300 mV was conducted to examine the electrochemical stability of Co_9S_8/Co_3O_4 (Fig. 4g). The sample clearly shows a steady state up to 20 h of the measurement. The surface morphology maintains after cycling test (inset SEM image in Fig. 4g), suggesting the structure stability of Co_9S_8/Co_3O_4. Furthermore, the long-term durability of Co_9S_8/Co_3O_4 was also evaluated by CV tests in a potential range of 0.8-2.0 V (*vs.* RHE) at a scan rate of 0.1 V s^{-1}. After 1000 cycles, no obvious shift or shape change of CV curves is observed, suggesting the high durability of the sample. Closely CV observation shows an oxidation peak at ~1.52 V, which can be ascribed to the reconstructed Co^{4+} species on the surface of Co_9S_8/Co_3O_4.[34] The Raman spectrum of Co_9S_8/Co_3O_4 after CV cycling test shows a broad peak at 576 cm^{-1} (Fig. S19), suggesting the presence of CoO_2 species.[34, 35] The peaks at 610 cm^{-1} and 472 cm^{-1} can be ascribed to Co_3O_4 and Co_9S_8, respectively.[11, 36] For Co_3O_4, Co/Co_3O_4 and Co_9S_8, CV cycling curves show a bit shift indicating a less stable structure of these catalysts (Figs. S20a, d and g). The peaks at 1.47 V and 1.37 V corresponding to the oxidation of Co from Co^{2+}/Co^{3+} and Co^{3+}/Co^{4+} can be observed in the CV cycling curves, suggesting the in-situ formation of CoOOH and Co^{4+} species on the surface of Co_3O_4 and Co/Co_3O_4, respectively.[34, 37] CV curves of Co_9S_8 exhibit anodic peaks at 1.15 V and 1.37 V due to the oxidation of Co^{+} to Co^{2+} and Co^{2+} to Co^{3+}, respectively. The CV result indicates the in-situ formation of $Co(OH)_2$ on the surface of Co_9S_8, and further reconstructed to CoOOH before the OER process. As shown in Figs. S20c, f and i, the Raman bands located at 465 (464) cm^{-1} and 673 (664) cm^{-1} demonstrate the presence of CoOOH in the Co_3O_4, Co/Co_3O_4 and Co_9S_8.[38]

The exceptional OER performance of Co_9S_8/Co_3O_4 can be assigned to the synergetic effect of the diverse porous architecture and heterojunction structures. On the one hand, the diverse

porous architecture contains macropores and mesopores, where macropores provide quick pathways for reactant and product, and mesopores can contribute more active sites on the surface. On the other hand, the intimate combination of Co_9S_8 and Co_3O_4 lead to the formation of a heterojunction interface, which is favorable for generating active sites as well as the fast charge transport.[39, 40] The interference between two different components induces interfacial electron redistribution and tune the surface charge state, which promotes the OER dynamic kinetics.[41] Importantly, fast charge transport induced by heterostructure will stimulate and stabilize Co^{4+} species (CoO_2) on the surface of Co_9S_8/Co_3O_4, which can reduce the energy barrier of the potential-determining step and thereby enhance the OER performance.[34] In addition, the presence of abundant oxygen vacancies (O_V) in Co_9S_8/Co_3O_4 can modify the absorption/desorption of electrocatalysts with the reactants as well as the electronic structure and electronic conductivity of the catalysts, thus promoting the OER activities.[42]

CONCLUSION

To sum up, a facile hydrometallurgy and thermal treatment were applied to regenerate Co-based electrocatalysts from spent LCO cathode materials. Thermal temperature and atmosphere are optimized to control the microstructure and composition of the Co-based catalysts. As a result, Co_9S_8/Co_3O_4 obtained via a sulfidation process (450 ℃, 2h) exhibited desirable OER activities (η_{10}=274 mV, Tafel slope=48.7 mV dec^{-1}), outperforming Co_3O_4 (η_{10}=342 mV, Tafel slope=70.5 mV dec^{-1}), Co/Co_3O_4 (η_{10}=298 mV, Tafel slope=58.6 mV dec^{-1}) and even the commercial RuO_2 (η_{10}=293 mV, Tafel slope=57.6 mV dec^{-1}). The enhanced OER performance can be mainly ascribed to the hierarchical porous architecture and heterojunction structures, which provide

enhanced active sites for boosting reaction kinetics. This study demonstrated an appropriate strategy for designing effective catalysts from the battery waste. Additionally, the successful regeneration of Co-based materials not only saves the valuable Co and Li resources, but also reduce environmental pollution.

ASSOCIATED CONTENT

Supporting Information.

The Supporting Information is available online or from the author.

ICP of Li leaching efficiency, SEM images and XRD patterns of air-annealed, N_2/10 vol% H_2-annealed and thioacetamide-treated samples, LSV curves, CV curves, ECSA results and Raman spectra of air-annealed, N_2/10 vol% H_2-annealed and thioacetamide-treated samples

Author Contributions

H. Bian designed the idea, carried out the experiments and wrote the paper. Z. Zhang, X-Y Lu and C. Liu supervised the experiment. W. Wu, X. Liao and J. Xu helped the material characterization and analysis. Y. Zhu helped dismantle the LIBs and electrode materials fabrication. C. Tsang and X-Y Lu revised the paper. All authors discussed the results and comments the manuscript.

Notes

The authors declare no conflict of interest.

ACKNOWLEDGMENT

Dr. Xiao-ying Lu would like to thank the financial support from Hong Kong Environment and Conservation Fund (No.: 39/2019). We also acknowledge the financial supports from the National Natural Science Foundation of China (21905180), the Shenzhen Sci. & Tech. research grant (JCYJ20180305124237416), Natural Science Foundation of Guangdong Province (2022A1515011438). Instrumental Analysis Center of Shenzhen University (Lihu Campus) was appreciated for material characterizations. Thanks eceshi (www.eceshi.com) for the XPS test.

REFERENCES

1. Zhang, B.; Xie, H.; Lu, B.; Chen, X.; Xing, P.; Qu, J.; Song, Q.; Yin, H., A Green Electrochemical Process to Recover Co and Li from Spent $LiCoO_2$-Based Batteries in Molten Salts. *ACS Sustainable Chem. Eng.* **2019,** *7* (15), 13391-13399.

2. Fan, E.; Li, L.; Wang, Z.; Lin, J.; Huang, Y.; Yao, Y.; Chen, R.; Wu, F., Sustainable Recycling Technology for Li-Ion Batteries and Beyond: Challenges and Future Prospects. *Chem. Rev.* **2020,** *120* (14), 7020-7063.

3. Lithium market-growth, trends, covid-19 impact, and forecasts (2022-2027). https://mordorintelligence.com/industry-reports/lithium-market.

4. Hu, X.; Mousa, E.; Ye, G., Recovery of Co, Ni, Mn, and Li from Li-ion batteries by smelting reduction - Part II: A pilot-scale demonstration. *J. Power Sources* **2021,** *483*, 229089.

5. Wang, Y.; An, N.; Wen, L.; Wang, L.; Jiang, X.; Hou, F.; Yin, Y.; Liang, J., Recent progress on the recycling technology of Li-ion batteries. *Journal of Energy Chemistry* **2021,** *55*, 391-419.

6. Watkins, E.; Farmer, A. *Managing waste batteries from electric vehicles: The case of the*

European Union and the Republic of Korea; Institute for European Environmental Policy: Institute for European Environmental Policy, 2021.

7. Tao, R.; Xing, P.; Li, H.; Sun, Z.; Wu, Y., Recovery of spent $LiCoO_2$ lithium-ion battery via environmentally friendly pyrolysis and hydrometallurgical leaching. *Resour. Conserv. Recycl.* **2022,** *176*, 105921.

8. From Trading Economics. https://tradingeconomics.com/.

9. Han, L.; Dong, S.; Wang, E., Transition-Metal (Co, Ni, and Fe)-Based Electrocatalysts for the Water Oxidation Reaction. *Adv. Mater.* **2016,** *28* (42), 9266-9291.

10. Tang, Y.; Shen, K.; Zheng, J.; He, B.; Chen, J.; Lu, J.; Ge, W.; Shen, L.; Yang, P.; Deng, S., d-Band center modulating of CoO_x/Co_9S_8 by oxygen vacancies for fast-kinetics pathway of water oxidation. *Chem. Eng. J.* **2022,** *427*, 130915.

11. Hu, Z.; Hao, L.; Quan, F.; Guo, R., Recent developments of Co_3O_4-based materials as catalysts for the oxygen evolution reaction. *Catalysis Science & Technology* **2022,** *12* (2), 436-461.

12. Anantharaj, S.; Ede, S. R.; Sakthikumar, K.; Karthick, K.; Mishra, S.; Kundu, S., Recent Trends and Perspectives in Electrochemical Water Splitting with an Emphasis on Sulfide, Selenide, and Phosphide Catalysts of Fe, Co, and Ni: A Review. *ACS Catal.* **2016,** *6* (12), 8069-8097.

13. Zhang, S. L.; Guan, B. Y.; Lu, X. F.; Xi, S.; Du, Y.; Lou, X. W., Metal Atom-Doped Co_3O_4 Hierarchical Nanoplates for Electrocatalytic Oxygen Evolution. *Adv. Mater.* **2020,** *32* (31), 2002235.

14. Wang, L.; Duan, X.; Liu, X.; Gu, J.; Si, R.; Qiu, Y.; Qiu, Y.; Shi, D.; Chen, F.; Sun, X.; Lin, J.; Sun, J., Atomically Dispersed Mo Supported on Metallic Co_9S_8 Nanoflakes as an

Advanced Noble-Metal-Free Bifunctional Water Splitting Catalyst Working in Universal pH Conditions. *Adv. Energy Mater.* **2020,** *10* (4), 1903137.

15. Sun, L.; Qiu, K., Organic oxalate as leachant and precipitant for the recovery of valuable metals from spent lithium-ion batteries. *Waste Manage. (Oxford)* **2012,** *32* (8), 1575-1582.

16. Li, Y.; Li, F.-M.; Meng, X.-Y.; Li, S.-N.; Zeng, J.-H.; Chen, Y., Ultrathin Co_3O_4 Nanomeshes for the Oxygen Evolution Reaction. *ACS Catal.* **2018,** *8* (3), 1913-1920.

17. Peng, H.; Zhang, W.; Song, Y.; Yin, F.; Zhang, C.; Zhang, L., In situ construction of Co/Co_3O_4 with N-doped porous carbon as a bifunctional electrocatalyst for oxygen reduction and oxygen evolution reactions. *Catal. Today* **2020,** *355*, 286-294.

18. Qi, J.; Zhang, W.; Cao, R., Aligned cobalt-based $Co@CoO_x$ nanostructures for efficient electrocatalytic water oxidation. *Chem. Commun.* **2017,** *53* (66), 9277-9280.

19. Zhang, P.; Cai, Z.; You, S.; Wang, F.; Dai, Y.; Zhang, C.; Zhang, Y.; Ren, N.; Zou, J., Self-generated carbon nanotubes for protecting active sites on bifunctional Co/CoO_x schottky junctions to promote oxygen reduction/evolution reactions via efficient valence transition. *J. Colloid Interface Sci.* **2019,** *557*, 580-590.

20. Zhao, Y.; Fu, Q.; Wang, D.; Pang, Q.; Gao, Y.; Missiul, A.; Nemausat, R.; Sarapulova, A.; Ehrenberg, H.; Wei, Y.; Chen, G., Co_9S_8@carbon yolk-shell nanocages as a high performance direct conversion anode material for sodium ion batteries. *Energy Storage Materials* **2019,** *18*, 51-58.

21. Liu, J.; Ke, J.; Li, Y.; Liu, B.; Wang, L.; Xiao, H.; Wang, S., Co_3O_4 quantum dots/TiO_2 nanobelt hybrids for highly efficient photocatalytic overall water splitting. *Appl. Catal., B* **2018,** *236*, 396-403.

22. Wang, X.; He, Y.; Han, X.; Zhao, J.; Li, L.; Zhang, J.; Zhong, C.; Deng, Y.; Hu, W.,

Engineering cobalt sulfide/oxide heterostructure with atomically mixed interfaces for synergistic electrocatalytic water splitting. *Nano Res.* **2022,** *15* (2), 1246-1253.

23. Xiang, K.; Song, Z.; Wu, D.; Deng, X.; Wang, X.; You, W.; Peng, Z.; Wang, L.; Luo, J.-L.; Fu, X.-Z., Bifunctional Pt–Co_3O_4 electrocatalysts for simultaneous generation of hydrogen and formate via energy-saving alkaline seawater/methanol co-electrolysis. *J. Mater. Chem. A* **2021,** *9* (10), 6316-6324.

24. Zhong, J.; Zeng, Y.; Zhang, M.; Feng, W.; Xiao, D.; Wu, J.; Chen, P.; Fu, M.; Ye, D., Toluene oxidation process and proper mechanism over Co_3O_4 nanotubes: Investigation through in-situ DRIFTS combined with PTR-TOF-MS and quasi in-situ XPS. *Chem. Eng. J.* **2020,** *397*, 125375.

25. Cong, L.; Zhang, S.; Zhu, H.; Chen, W.; Huang, X.; Xing, Y.; Xia, J.; Yang, P.; Lu, X., Structure-design and theoretical-calculation for ultrasmall Co_3O_4 anchored into ionic liquid modified graphene as anode of flexible lithium-ion batteries. *Nano Res.* **2022,** *15* (3), 2104-2111.

26. Wang, C.; Li, Y.; Gu, C.; Zhang, L.; Wang, X.; Tu, J., Active Co@CoO core/shell nanowire arrays as efficient electrocatalysts for hydrogen evolution reaction. *Chem. Eng. J.* **2022,** *429*, 132226.

27. Wang, Y.; Zhu, T.; Zhang, Y.; Kong, X.; Liang, S.; Cao, G.; Pan, A., Rational design of multi-shelled CoO/Co_9S_8 hollow microspheres for high-performance hybrid supercapacitors. *J. Mater. Chem. A* **2017,** *5* (35), 18448-18456.

28. Wang, J.; Li, L.; Chen, X.; Lu, Y.; Yang, W., Monodisperse cobalt sulfides embedded within nitrogen-doped carbon nanoflakes: an efficient and stable electrocatalyst for the oxygen reduction reaction. *J. Mater. Chem. A* **2016,** *4* (29), 11342-11350.

29. Guo, M.; Liu, Y.; Dong, S.; Jiao, X.; Wang, T.; Chen, D., Co_9S_8-Catalyzed Growth of

Thin-Walled Graphite Microtubes for Robust, Efficient Overall Water Splitting. *ChemSusChem* **2018,** *11* (23), 4150-4155.

30. Cao, Z.-q.; Wu, M.-z.; Hu, H.-b.; Liang, G.-j.; Zhi, C.-y., Monodisperse Co_9S_8 nanoparticles in situ embedded within N, S-codoped honeycomb-structured porous carbon for bifunctional oxygen electrocatalyst in a rechargeable Zn–air battery. *NPG Asia Materials* **2018,** *10* (7), 670-684.

31. Chu, H.; Zhang, D.; Feng, P.; Gu, Y.; Chen, P.; Pan, K.; Xie, H.; Yang, M., Engineering oxygen vacancies in $CoO@Co_3O_4$/C nanocomposites for enhanced electrochemical performances. *Nanoscale* **2021,** *13* (46), 19518-19526.

32. Huang, L.; Wei, M.; Zaman, S.; Ali, A.; Xia, B. Y., Well-connection of micro-platinum and cobalt oxide flower array with optimized water dissociation and hydrogen recombination for efficient overall water splitting. *Chem. Eng. J.* **2020,** *398*, 125669.

33. Zhao, G.; Rui, K.; Dou, S. X.; Sun, W., Heterostructures for Electrochemical Hydrogen Evolution Reaction: A Review. *Adv. Funct. Mater.* **2018,** *28* (43), 1803291.

34. Yao, N.; Wang, G.; Jia, H.; Yin, J.; Cong, H.; Chen, S.; Luo, W., Intermolecular Energy Gap-Induced Formation of High-Valent Cobalt Species in CoOOH Surface Layer on Cobalt Sulfides for Efficient Water Oxidation. *Angew. Chem. Int. Ed.* **2022,** *61* (28), e202117178.

35. Yu, M.; Budiyanto, E.; Tüysüz, H., Principles of Water Electrolysis and Recent Progress in Cobalt-, Nickel-, and Iron-Based Oxides for the Oxygen Evolution Reaction. *Angew. Chem. Int. Ed.* **2022,** *61* (1), e202103824.

36. Hou, T.; Jia, Z.; Wang, B.; Li, H.; Liu, X.; Bi, L.; Wu, G., MXene-based accordion 2D hybrid structure with Co9S8/C/Ti3C2Tx as efficient electromagnetic wave absorber. *Chem. Eng. J.* **2021,** *414*, 128875.

37. Bian, H.; Chen, T.; Chen, Z.; Liu, J.; Li, Z.; Du, P.; Zhou, B.; Zeng, X.; Tang, J.; Liu, C., One-step synthesis of mesoporous Cobalt sulfides (CoS_x) on the metal substrate as an efficient bifunctional electrode for overall water splitting. *Electrochim. Acta* **2021,** *389*, 138786.

38. Ghosh, S.; Mondal, A.; Tudu, G.; Ghosh, S.; Koppisetti, H. V. S. R. M.; Inta, H. R.; Saha, D.; Mahalingam, V., Efficient Electrochemical Reconstruction of a Cobalt- and Silver-Based Precatalytic Oxalate Framework for Boosting the Alkaline Water Oxidation Performance. *ACS Sustainable Chem. Eng.* **2022,** *10* (22), 7265-7276.

39. Zhu, C.; Wang, A.-L.; Xiao, W.; Chao, D.; Zhang, X.; Tiep, N. H.; Chen, S.; Kang, J.; Wang, X.; Ding, J.; Wang, J.; Zhang, H.; Fan, H. J., In Situ Grown Epitaxial Heterojunction Exhibits High-Performance Electrocatalytic Water Splitting. *Adv. Mater.* **2018,** *30* (13), 1705516.

40. Yan, H.; Xie, Y.; Wu, A.; Cai, Z.; Wang, L.; Tian, C.; Zhang, X.; Fu, H., Anion-Modulated HER and OER Activities of 3D Ni–V-Based Interstitial Compound Heterojunctions for High-Efficiency and Stable Overall Water Splitting. *Adv. Mater.* **2019,** *31* (23), 1901174.

41. Tran, N. Q.; Bui, V. Q.; Le, H. M.; Kawazoe, Y.; Lee, H., Anion–Cation Double Substitution in Transition Metal Dichalcogenide to Accelerate Water Dissociation Kinetic for Electrocatalysis. *Adv. Energy Mater.* **2018,** *8* (15), 1702139.

42. Zhu, K.; Shi, F.; Zhu, X.; Yang, W., The roles of oxygen vacancies in electrocatalytic oxygen evolution reaction. *Nano Energy* **2020,** *73*, 104761.

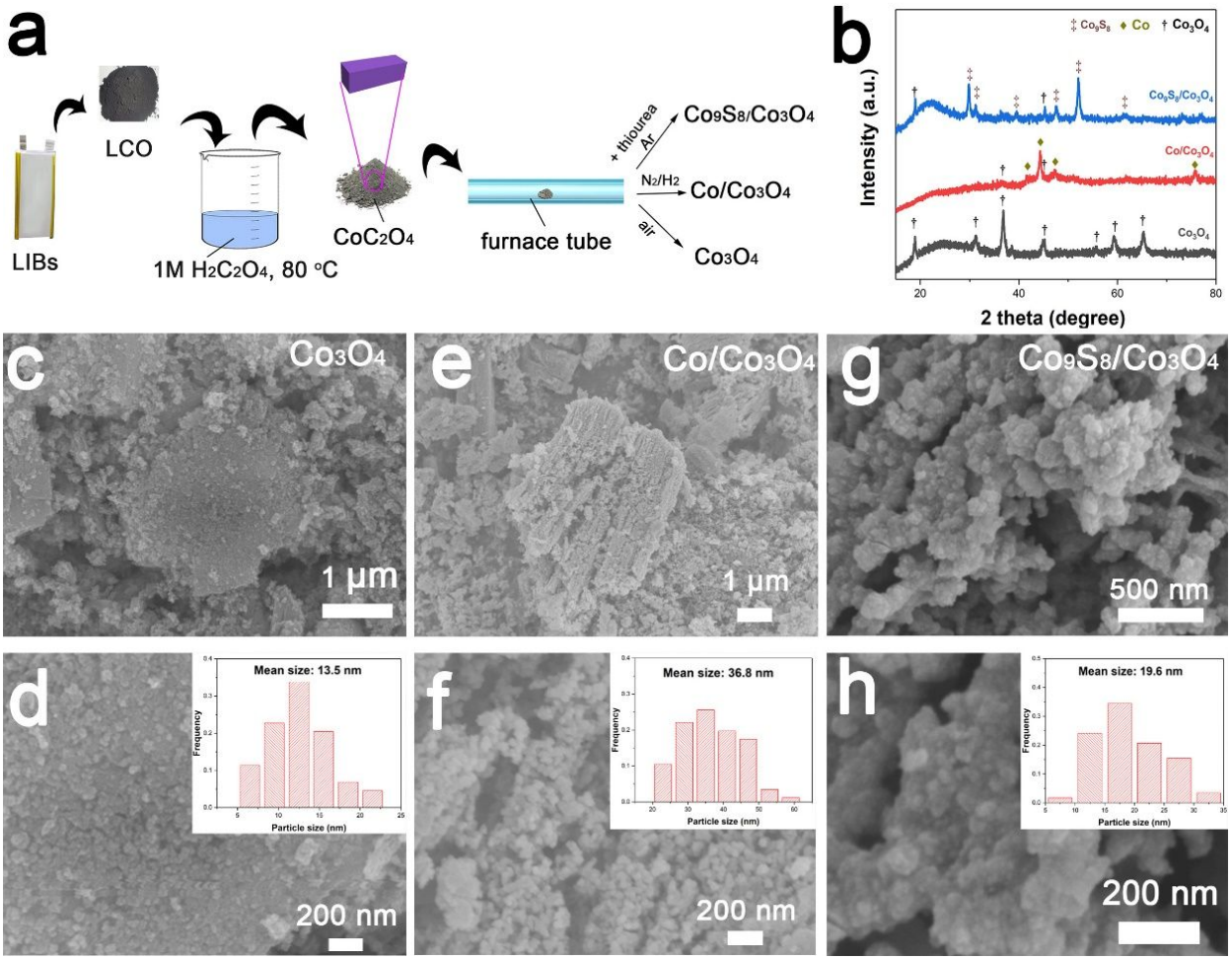

Fig. 1 a) Schematic illustration of recycling process of the spent LCO batteries to Co-based catalysts (Co_3O_4, Co/Co_3O_4 and Co_9S_8/Co_3O_4); b) XRD patterns of the prepared Co_3O_4, Co/Co_3O_4 and Co_9S_8/Co_3O_4; SEM images of c-d) Co_3O_4, e-f) Co/Co_3O_4 and g-h) Co_9S_8/Co_3O_4 at different magnifications. The insets show the statistic particle size of the corresponding samples.

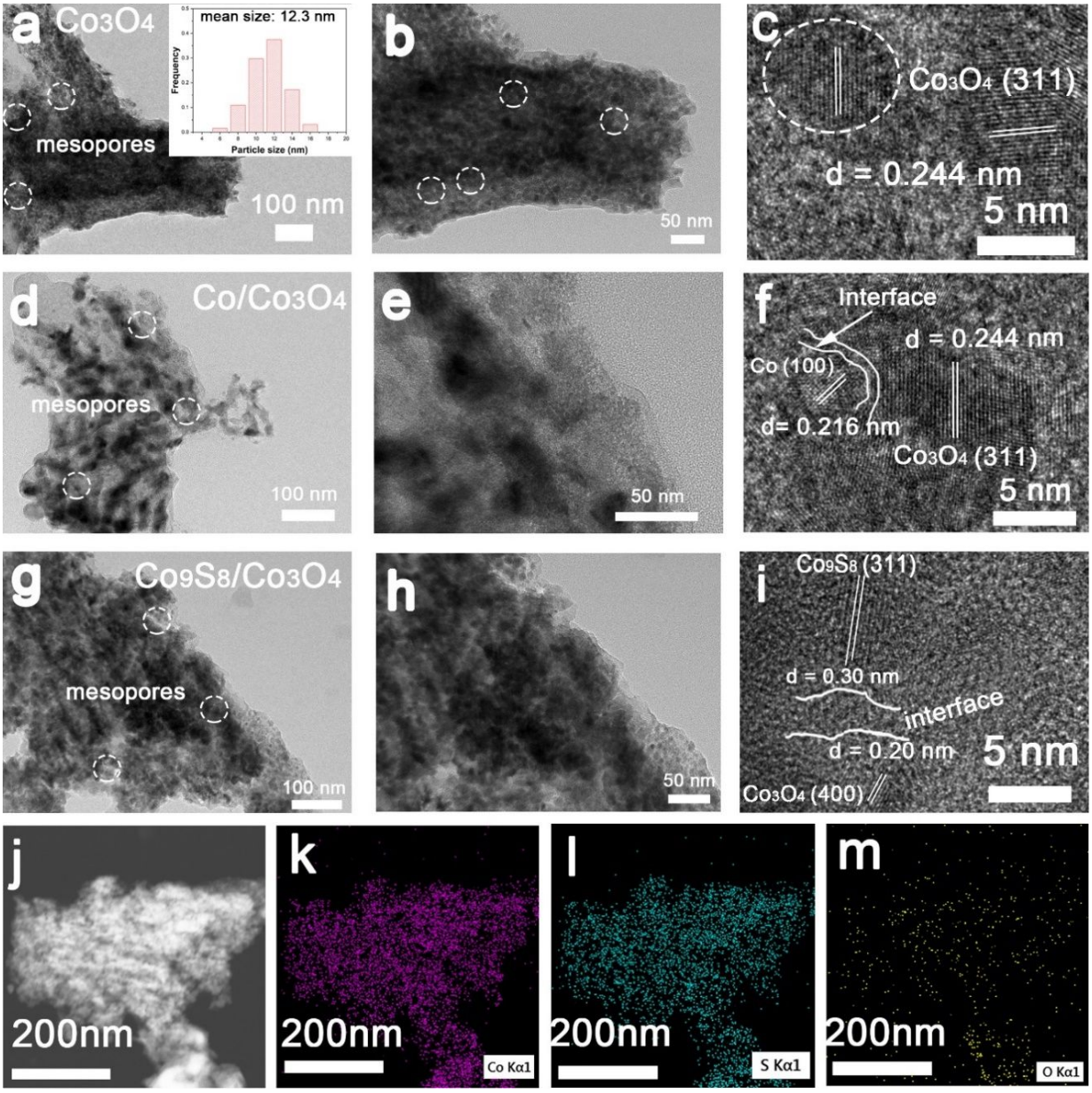

Fig. 2 TEM images of a-b) Co_3O_4, d-e) Co/Co_3O_4 and g-h) Co_9S_8/Co_3O_4, HRTEM images of c) Co_3O_4, f) Co/Co_3O_4 and i) Co_9S_8/Co_3O_4, and j-m) TEM image and elemental mapping images of Co_9S_8/Co_3O_4.

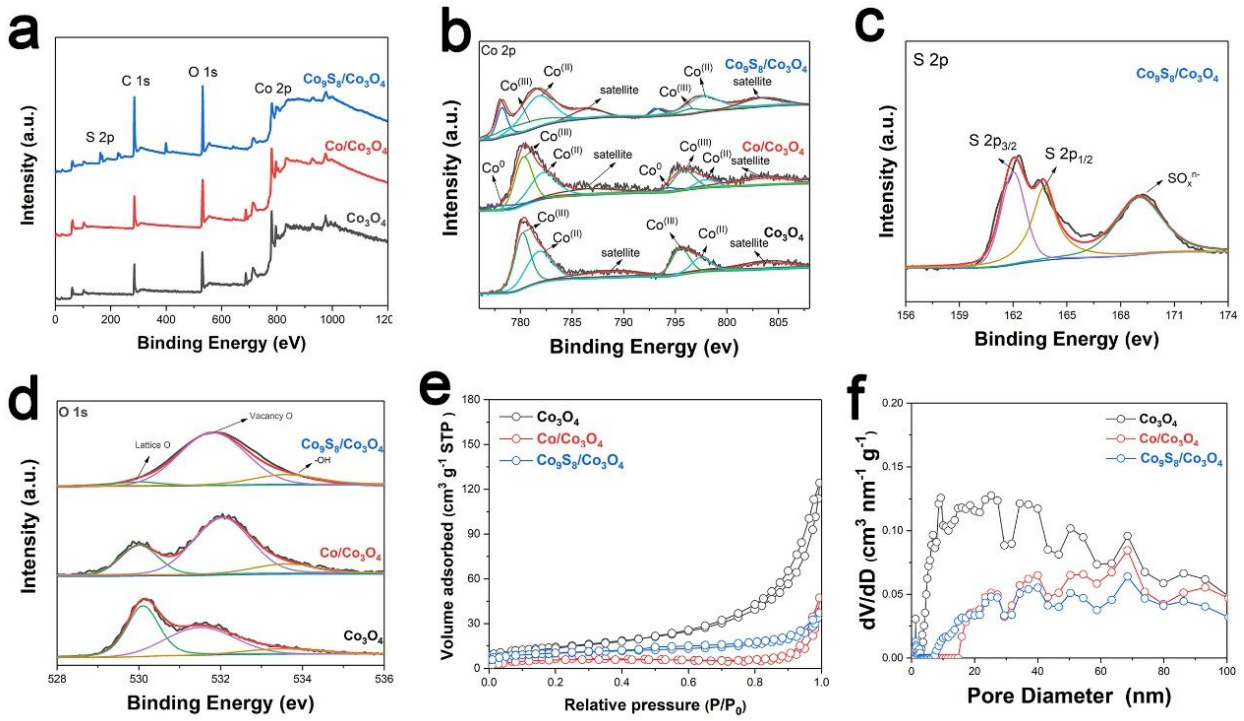

Fig. 3 a) XPS survey spectra, high-resolution Co2p (b), S2p (c) and O1s (d) XPS spectra, e) nitrogen adsorption-desorption isotherms and f) the corresponding pore size distribution of the prepared Co_3O_4, Co/Co_3O_4 and Co_9S_8/Co_3O_4.

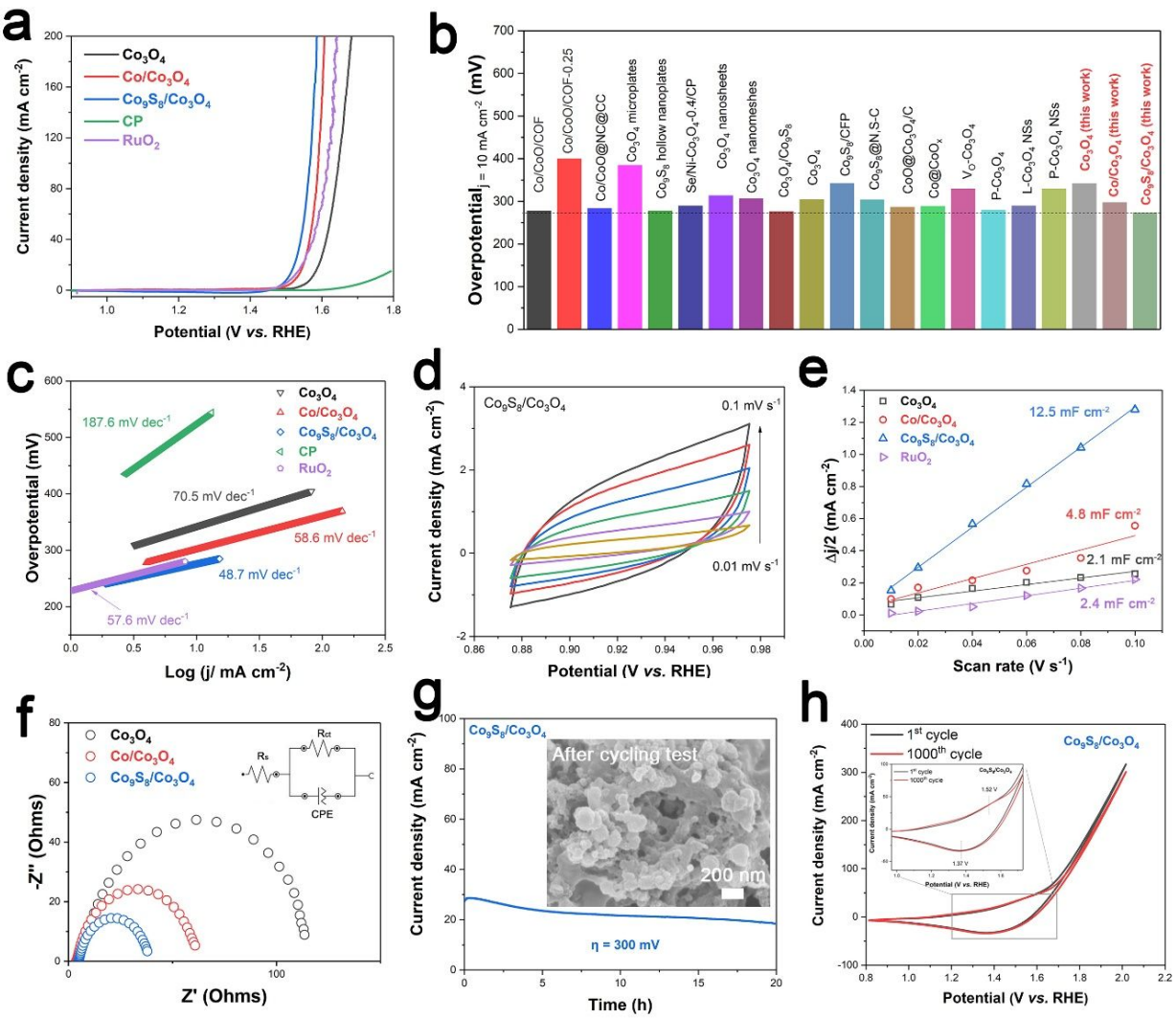

Fig. 4 Electrocatalytic OER activity of regenerated Co-based catalysts from the spent LCO batteries. a) IR-corrected polarization curves of the Co_3O_4, Co/Co_3O_4, Co_9S_8/Co_3O_4, RuO_2 and carbon paper (CP) in 1 M KOH electrolyte at a scan rate of 2 mV s^{-1}; b) Comparison result of η_{10} for our catalysts and other Co-based OER catalysts; c) Tafel plots of the catalysts obtained from their corresponding polarization curves; d) CV curves of Co_9S_8/Co_3O_4 at different scan rates from 0.01 to 0.1 V s^{-1}; e) Current densities versus scan rates measured at a potential value of 0.925 V (*vs.* RHE) for the obtained catalysts; f) Nyquist plots of the catalysts at an overpotential value of 300 mV for OER; g) The *I-t* curve of Co_9S_8/Co_3O_4 for OER process at an overpotential

of 300 mV for 20 h (the inset shows the morphology of the sample after long-term cycling test); h) CV cycling stability test of Co_9S_8/Co_3O_4 at a scan rate of 0.1 V s^{-1}.

TOC

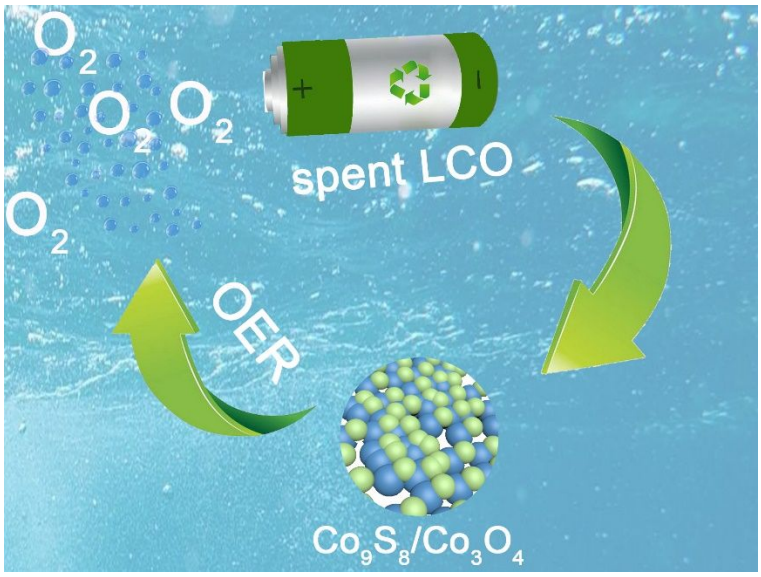

Waste to treasure: Regeneration of mesoporous Co_9S_8/Co_3O_4 heterostructures for efficient electrochemical oxygen evolution reaction.